Atmos. Meas. Tech., 9, 939–953, 2016
www.atmos-meas-tech.net/9/939/2016/
doi:10.5194/amt-9-939-2016

Atmospheric Measurement Techniques
Open Access
EGU

The airborne mass spectrometer AIMS – Part 1: AIMS-H_2O for UTLS water vapor measurements

Stefan Kaufmann[1], Christiane Voigt[1,2], Tina Jurkat[1], Troy Thornberry[3,4], David W. Fahey[3,4], Ru-Shan Gao[3], Romy Schlage[1], Dominik Schäuble[5], and Martin Zöger[6]

[1]Deutsches Zentrum für Luft- und Raumfahrt, Institut für Physik der Atmosphäre, Oberpfaffenhofen, Germany
[2]Johannes Gutenberg-Universität, Institut für Physik der Atmosphäre, Mainz, Germany
[3]NOAA Earth System Research Laboratory, Chemical Sciences Division, Boulder, Colorado, USA
[4]University of Colorado, CIRES, Boulder, Colorado, USA
[5]Institute for Advanced Sustainability Studies, Potsdam, Germany
[6]Deutsches Zentrum für Luft- und Raumfahrt, Flight Experiments, Oberpfaffenhofen, Germany

Correspondence to: Stefan Kaufmann (stefan.kaufmann@dlr.de)

Received: 27 November 2015 – Published in Atmos. Meas. Tech. Discuss.: 21 December 2015
Revised: 18 February 2016 – Accepted: 22 February 2016 – Published: 7 March 2016

Abstract. In the upper troposphere and lower stratosphere (UTLS), the accurate quantification of low water vapor concentrations has presented a significant measurement challenge. The instrumental uncertainties are passed on to estimates of H_2O transport, cloud formation and the role of H_2O in the UTLS energy budget and resulting effects on surface temperatures. To address the uncertainty in UTLS H_2O determination, the airborne mass spectrometer AIMS-H_2O, with in-flight calibration, has been developed for fast and accurate airborne water vapor measurements.

We present a new setup to measure water vapor by direct ionization of ambient air. Air is sampled via a backward facing inlet that includes a bypass flow to assure short residence times (< 0.2 s) in the inlet line, which allows the instrument to achieve a time resolution of ~ 4 Hz, limited by the sampling frequency of the mass spectrometer. From the main inlet flow, a smaller flow is extracted into the novel pressure-controlled gas discharge ion source of the mass spectrometer. The air is directed through the gas discharge region where ion–molecule reactions lead to the production of hydronium ion clusters, $H_3O^+(H_2O)_n$ ($n = 0, 1, 2$), in a complex reaction scheme similar to the reactions in the D-region of the ionosphere. These ions are counted to quantify the ambient water vapor mixing ratio. The instrument is calibrated during flight using a new calibration source based on the catalytic reaction of H_2 and O_2 on a Pt surface to generate a calibration standard with well-defined and stable H_2O mixing ratios. In order to increase data quality over a range of mixing ratios, two data evaluation methods are presented for lower and higher H_2O mixing ratios respectively, using either only the $H_3O^+(H_2O)$ ions or the ratio of all water vapor dependent ions to the total ion current. Altogether, a range of water vapor mixing ratios from 1 to 500 parts per million by volume (ppmv) can be covered with an accuracy between 7 and 15 %. AIMS-H_2O was deployed on two DLR research aircraft, the Falcon during CONCERT (CONtrail and Cirrus ExpeRimenT) in 2011, and HALO during ML-CIRRUS (Mid-Latitude CIRRUS) in 2014. The comparison of AIMS-H_2O with the SHARC tunable diode laser hygrometer during ML-CIRRUS shows a correlation near to 1 in the range between 10 and 500 ppmv for the entire campaign.

1 Introduction

Airborne mass spectrometry is a powerful tool for the fast and accurate measurement of various trace gases relevant for atmospheric chemistry and climate. Linear quadrupole mass spectrometers (LQMS) can be operated in a variety of configurations – e.g., for direct measurements of ions in the atmosphere (Viggiano, 1993; McCrumb and Arnold, 1981), chemical ionization mass spectrometry (CIMS) (e.g., Huey and Lovejoy, 1996), proton-transfer-reaction mass spectrometry (PTR-MS) (Hansel et al., 1995) or artificial ionization and

characterization of ambient air (Thornberry et al., 2013). In contrast to the other two techniques, CIMS and PTR-MS utilize transfer reactions between artificially produced reagent ions and ambient air molecules. The Atmospheric Ionization Mass Spectrometer (AIMS) described in this work makes use of the three latter techniques. Part 1 of this paper focuses on the measurement of water vapor down to low mixing ratios typical for the lower stratosphere by direct ionization of ambient air. In Part 2 (Jurkat et al., 2016), the setup and measurements using the CIMS technique with SF_5^- chemistry for the set of trace gases HCl, HNO_3, HNO_2, SO_2 and $ClONO_2$ are presented.

The water vapor configuration of AIMS, referred to as AIMS-H_2O, was developed in response to the large discrepancies between different airborne H_2O measurements that have been found in the past (Oltmans et al., 2000). Accurate knowledge of water vapor concentrations in the atmosphere is crucial for understanding Earth's climate since it is the most important greenhouse gas and engages in a positive feedback in the climate system (e.g., Manabe and Wetherald, 1967; Kiehl and Trenberth, 1997). The radiative impact of changes in water vapor concentrations is particularly strong in the tropopause region and in the lower stratosphere (Solomon et al., 2010; Riese et al., 2012) where water vapor mixing ratios are in the range of only a few parts per million by volume (ppmv, 10^{-6} mol mol^{-1}). Measurements in these regions, in situ as well as satellite-based instruments, showed significant discrepancies in the past with offsets of the order of several 10 % (e.g., Weinstock et al., 2009; Vömel et al., 2007). These uncertainties in UTLS water vapor concentrations directly transfer into the calculation of the atmosphere's energy budget (Forster and Shine, 2002). In addition, these uncertainties currently limit our understanding of microphysical processes related to ice nucleation, growth and persistence of cirrus clouds in the upper troposphere (Krämer et al., 2009; Jensen et al., 2005; Heymsfield and Miloshevich, 1995) and the tropical UTLS region (Jensen et al., 1994). In turn, this affects the quantification of the tropical H_2O transport to the stratosphere (Dinh et al., 2014) and the UTLS radiation budget, including the effect of clouds (Ramanathan et al., 1989; Sassen and Comstock, 2001; Liou, 1986; Dinh and Fueglistaler, 2014).

To address the disagreements in UTLS water vapor measurements, a series of laboratory and field campaigns has been launched, one of the first being the AquaVIT-I experiment in 2007 (Fahey et al., 2014) at the AIDA cloud chamber in Karlsruhe. In the lab, discrepancies between the instruments were found to be smaller than in the field but still above ±10 % especially at water vapor mixing ratios below 10 ppmv. The instrument performance and improvements have been re-evaluated in two follow-up experiments, AquaVIT-II and III in 2013 and 2015 (not published yet). In order to assess the technical improvements not only in the laboratory but also in the atmosphere, an extensive comparison of in situ hygrometers was performed during the airborne field mission MACPEX (Mid-latitude Airborne Cirrus Properties EXperiment) in 2011. Although the performance of in situ water vapor instruments has improved over the last decade (Rollins et al., 2014; Meyer et al., 2015), the accuracy of airborne water vapor measurements in the tropopause region still remains an issue of concern.

With the mass spectrometer AIMS-H_2O, which includes in-flight calibration, we have developed a significant contribution to the field of airborne water vapor measurements with a focus on the low H_2O mixing ratios of the UTLS. The instrument was deployed on an aircraft for the first time during the CONCERT (CONtrail and Cirrus ExpeRimenT) experiment with the DLR Falcon in 2011 (Kaufmann et al., 2014). After further development, AIMS-H_2O was deployed on HALO during ML-CIRRUS (Midlatitude CIRRUS) in 2014. Its twin configuration, AIMS-TG for trace gas observations, has also been operated on the DLR Falcon during CONCERT (Voigt et al., 2014) and on HALO during TACTS/ESMVal (Transport And Composition in the UT/LMS/Earth System Model Validation) in 2012 (Jurkat et al., 2014).

In this work, we first describe the mechanical and electrical setup of AIMS-H_2O with a special emphasis on the novel gas discharge ion source designed for the direct ionization of ambient water vapor. Second, we present the in-flight calibration setup and performance that is used to assure accurate and reliable airborne measurements. After a discussion of data reduction methods used to quantify ambient H_2O mixing ratios, we derive the instrumental uncertainties and present the first airborne measurements on HALO during ML-CIRRUS including a comparison with the Sophisticated Hygrometer for Atmospheric ResearCh (SHARC) in situ tunable diode laser hygrometer.

2 Setup of the mass spectrometer

AIMS consists of a linear quadrupole mass spectrometer (Huey et al., 1995) which was designed and built by THS instruments at the Georgia Institute of Technology (Greg Huey, Atlanta, USA). It is integrated in one HALO standard rack plus an external plate where the bypass pump is mounted (behind the rack in Fig. 1). The instrument is connected to a heated HALO Trace Gas Inlet (TGI, enviscope GmbH, Germany) and can be operated with either a backward- or forward-facing inlet geometry in order to sample the gas phase only or the sum of the gas phase and condensed phase (evaporated), respectively. In order to ensure a low residence time in the inlet line and thereby reduce inlet artifacts, a bypass flow of up to 30 standard liters per minute (standard L min^{-1}) is established using an IDP-3 scroll pump (Agilent Technologies, USA) (Fig. 2). The general flight setup of the mass spectrometer is described below following the gas flow from the inlet line through the pressure-regulated ionization chamber to the vacuum chamber of the mass spectrometer.

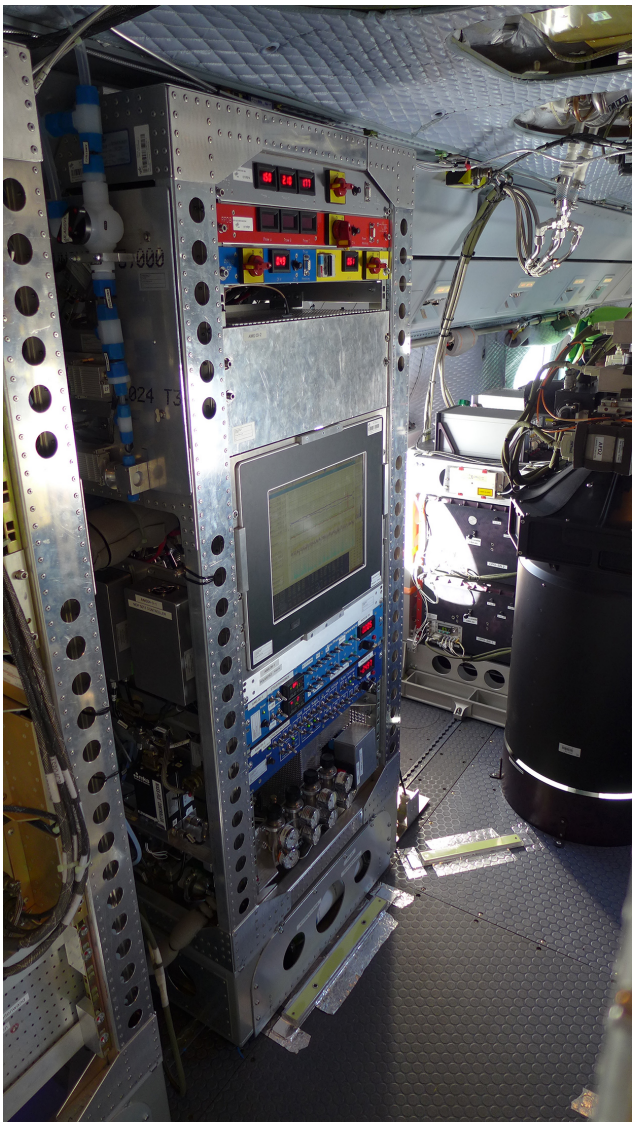

Figure 1. Front view of instrument rack in AIMS-H_2O configuration integrated in a HALO standard rack. The inlet line is connected to a trace gas inlet (TGI) mounted at the top fuselage of the aircraft.

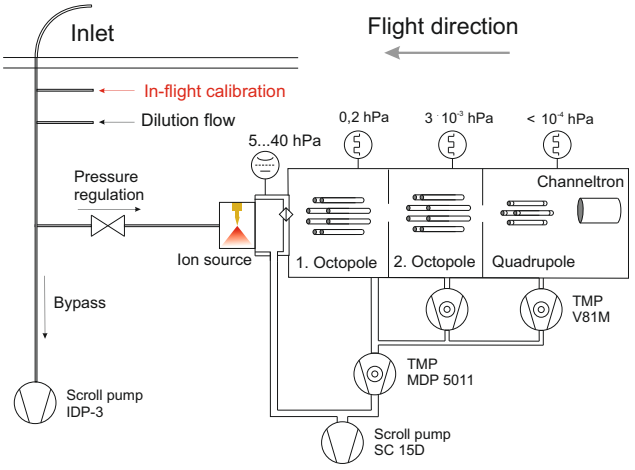

Figure 2. Schematic of the flight configuration of AIMS. Ambient air enters via a backward faced inlet and passes through a pressure regulation valve before entering the ion source. The detailed setup of the ion source for the two measurement modes is depicted in Fig. 5. The ion beam is then focused by two adjacent octopoles and finally separated by mass-to-charge ratio in the quadrupole. Additionally, connections for an optional dilution of ambient air and background measurements and for addition of trace gases for in-flight calibration (detail in Fig. 3) are mounted right beneath the inlet.

Details of the ion source and in-flight calibration techniques are presented separately in Sects. 3 and 4.

2.1 Inlet line

For the inlet line of AIMS-H_2O we use a Synflex composite tube (Data sheet Synflex 1300, www.goodrichsales.com/products/pdfs/1300.pdf) with an outer diameter of $1/2''$. The tube consists of an aluminum body with an inner ethylene copolymer film and an outer polyethylene jacket. The material combines several features which are of benefit for water vapor measurements in the aircraft. Adsorption of water vapor to the walls and diffusion through the walls of Synflex lines is comparable to stainless steel tubes. Furthermore, it is much more flexible than stainless steel tubing. An approximately 40 cm length of tube is fitted inside a HALO TGI and heated to 40 °C controlled by a bimetal switch. A 1.2 m length of tube is used to connect the TGI with the pressure regulation valve of AIMS-H_2O. Tubing connections are made using Swagelok stainless steel compression fittings. This part of the tubing is heated separately to 40 °C using a two-point temperature controller. Two tee fittings are integrated into the sample line as depicted in Fig. 2. The one directly at the TGI is used to add calibration gas, and the second one is used for an optional dilution flow with dry synthetic air (Air Liquide GmbH, residual H_2O, ~ 0.5 ppmv). The dilution flow is added via a mass flow controller (Type 1179, MKS Instruments) allowing for dilution ratios up to 2 : 1. A third tee fitting allows subsampling of air into the instrument while the large inlet flow needed for measurements with high time resolution flows directly to the pump. Since the two configurations of AIMS require specific properties of the inlet line, two different tubing sets are installed in the aircraft: Synflex and stainless steel for AIMS-H_2O and fluoropolymers (PFA) for AIMS-TG.

2.2 Pressure regulation

In order to guarantee constant flow and pressure conditions in the ion source, flow reactor and mass spectrometer, we use an automatically controlled pressure regulation valve mounted upstream of the ion source (Fig. 2). For AIMS-H_2O, the ball valve consists of stainless steel with a modified PTFE

(D1710 Type 1) sealing (Swagelok SS-42GS4). The pressure regulation has to be fast since it needs to compensate for rapid ambient pressure changes during aircraft ascent and descent between 1000 and 150 hPa, but it also has to be both precise and accurate since the reaction time for the ion–molecule reactions in the flow reactor scales linearly with the pressure. The lever of the manual valve was replaced by an adapter to control the valve using a servomotor (DA 22-30-4128, Volz Servos GmbH, Germany). The motor is controlled by a PID controller regulating the pressure measured by a Baratron manometer (MKS Instruments, Type 727) in the flow reactor. For AIMS-H_2O, 99 % of the measured pressure values have a deviation of less than 0.02 hPa (0.5 %) from the nominal value of 4.3 hPa. The pressure regulation can compensate for pressure changes during regular flight maneuvers like ascent and descent and thus contributes only a minor error source for the overall measurement.

2.3 Vacuum chamber

The instrument flow path downstream of the pressure-regulating valve consists of the ion source, the flow tube and three differentially pumped chambers which are connected by pinholes of different sizes. As indicated in Fig. 2 the pressure decreases from a few hPa in the ion source to less than 10^{-4} hPa in the last chamber containing the quadrupole and electron multiplier. The two chambers directly downstream of the ion source are equipped with two separate octopoles which act as lenses for the ion beam. Their main purpose is to focus the ion beam towards the quadrupole chamber. The first octopole is pumped by a MDP5011 molecular drag pump (Pfeiffer), the second one by a V-81M turbo pump (Agilent Technologies, USA). As backing pump for the MDP, we use a SC15D scroll pump (Oerlikon Leybold Vacuum GmbH). Separate DC electrical potentials (-250 to $+250$ V) can be applied to each aperture and the octopoles in order to accelerate or decelerate the ion current. This is of special importance in the first octopole chamber with a higher pressure where the acceleration of ions relative to the neutral gas molecules determines the fragmentation of ion–molecule clusters. For that reason, this chamber is also referred to as the Collision Dissociation Chamber (CDC). The aperture plate between the first and second octopole chamber is connected to ground, so all potentials applied to octopoles and apertures are relative to this aperture plate.

The third chamber, also pumped by a V-81M, contains the linear quadrupole (GP-203D, Extrel CMS, USA). Here, the ions are separated by their mass to charge ratio. Therefore both a DC and a high voltage RF potential are applied to the quadrupole rods so that only ions with the same mass-to-charge ratios can pass through the quadrupole on a stable trajectory at a time. Stray fields in entrance and exit areas of the quadrupole are minimized by pre- and post-filters, which themselves are short quadrupole rods at different potentials. The separated ion species are detected by an electron multiplier (Channeltron, ITT Ceramax 7550M, ITT Power Solutions) which counts single ion impacts (up to $\sim 4 \times 10^6\,s^{-1}$).

The quadrupole can be operated in two different measurement modes. The so-called "hop mode" is used to obtain time series of a few fixed mass-to-charge ratios. In this mode, the quadrupole repeatedly steps through up to 16 fixed mass-to-charge ratios with an integration time of the order of 100 ms each. For in-flight measurements, we are predominantly interested in the time dependence of known species, so the hop mode is the default measurement mode. The second mode is the "scan mode", in which the quadrupole potentials are increased continuously in order to obtain a mass spectrum as shown in Fig. 6. Depending on the step width, the time needed to record one spectrum is of the order of 30 s. Such spectra can be performed manually or automatically at specific time intervals in order to check for unexpected product ions during flight.

3 In-flight calibration

Since the environmental conditions during aircraft measurements are rather extreme in terms of changing pressure and temperature compared to the relatively stable conditions in the laboratory, it is always difficult to judge how a ground calibration transfers to in-flight conditions. In order to achieve highly accurate measurements, it is therefore important to calibrate during flight for the measured substances. However, there remains a tradeoff between higher accuracy achieved by a thorough in-flight calibration and the loss of precious (airborne) sampling time. The methods for in-flight calibration thus have to be fast, they need to be integrated in the airborne instrument setup and they need to be able to produce trace gas amounts typical for the investigated atmospheric conditions in a stable manner.

The in-flight calibration for the water vapor measurement is realized by the catalytic reaction of H_2 and O_2 on a Pt-surface in order to create a calibration flow with well-defined H_2O mixing ratios (Rollins et al., 2011). This technique was applied in flight for the first time during the MACPEX mission in 2011 (Thornberry et al., 2013). A mixture of (420 ± 8.4) ppmv H_2 in synthetic air (Airliquide GmbH) is stored in a 150 mL stainless steel cylinder (Swagelok) with a maximum pressure of 150 bar (Fig. 3). The cylinder can be refilled after each flight via a quick connector, thus for each flight 22.5 standard L of calibration gas are available. After the pressure regulator (2 bar), the H_2/ zero air mixture flows over a Pt mesh (Sigma-Aldrich, Prod.-Nr. 298107) which is folded inside a $1/4''$ stainless steel tube (Swagelok) and heated to 250 °C. In laboratory studies similar to the approach of Rollins et al. (2011), the plateau where the conversion efficiency (CE = ratio between H_2 mixing ratio before and H_2O mixing ratio after the catalyst) is stable above 95 % is reached at around 150 °C. The operating temperature of the catalyst is chosen to be high enough so that the CE is in-

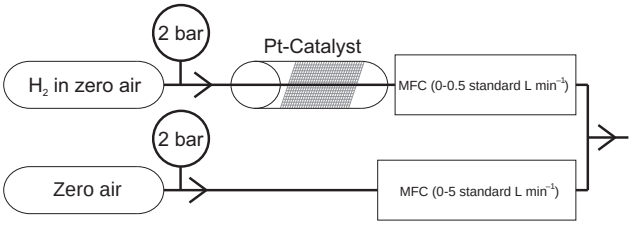

Figure 3. Setup of the in-flight calibration: **(a)** zero air can be added to the sample flow for dilution and background measurements. **(b)** A mixture of H_2 in zero air is passed over a heated Pt-catalyst and reacts to H_2O for calibration of the water vapor configuration. The water vapor mixing ratio in the calibration gas can be further adjusted by dilution with synthetic air from **(a)**. To allow for equilibration of the catalytic source, the calibration gas flow is switched on early and guided to the exhaust line before starting a calibration sequence.

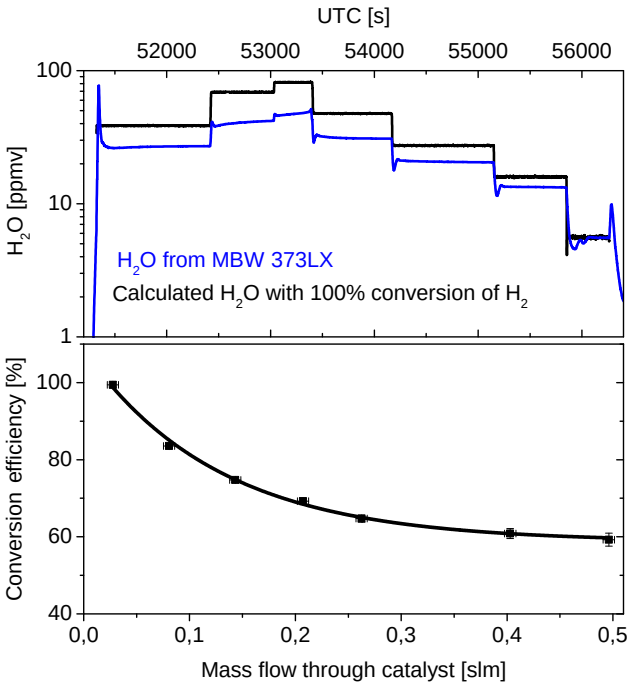

Figure 4. Performance of the calibration source with respect to the MBW 373LX reference instrument. The upper panel shows the expected H_2O mixing ratio calculated from the H_2 concentration in the gas cylinder and the gas flow through the catalyst assuming a complete conversion of every H_2 molecule into H_2O (black line). The blue line is the H_2O mixing ratio which was simultaneously measured by the dew point mirror. From the discrepancy between both lines we can calculate the conversion efficiency (CE) of the catalyst. The CE decreases with increasing flow through the catalyst and is fitted with an exponential function.

dependent of the exact catalyst temperature. It is important to operate the system at temperatures well above this threshold since it was found that the temperature of the gas stream can be up to 35 °C lower than the controlled temperature measured at the outer wall of the catalyst tube. This temperature difference depends on the gas flow rate through the catalyst, which in our system is up to 0.5 standard L min^{-1}, the maximum range of the MFC (MKS Instruments, Type 1179A) right behind the catalyst. Since the in-flight calibration period should be kept as short as possible to maximize measurement time, the flow through the catalyst can alternatively be drained to the exhaust line. This allows the catalyst and tubing system to equilibrate before the calibration sequence is started.

At high temperature, the CE of the catalyst only depends on the available reaction sites on the Pt mesh and the flow through the catalyst tube. At higher flow, the CE decreases linearly with increasing flow rate since the mean residence time, and thus the potential available reaction time, is reduced. In order to increase the available reaction time, the MFC is located downstream of the catalyst tube as depicted in Fig. 3b so that the catalyst itself is exposed to a pressure of 2 bar. At flow rates below 0.06 standard L min^{-1}, the CE is 100 % within the uncertainties of H_2 mixing ratio, MFCs and the reference measurement. When increasing the flow up to the maximum of 0.5 standard L min^{-1}, the CE usually decreases down to around 60 % (Fig. 4). This behavior is found to be stable over the typical timescale of airborne measurement campaigns of a few weeks. To assure a reproducible performance of the calibration source, it is regularly characterized by ground measurements using an MBW 373-LX dew point mirror (MBW Calibration AG, Switzerland) as a reference instrument. Using the reference measurement, the flow dependency of the CE can be approximated by a exponential fit function (Fig. 4). This enables the use of the complete range of gas flows through the catalyst and thus a range of the in-flight calibration from (0.5 ± 0.1) ppmv up to (150 ± 9) ppmv H_2O. If the residence time of the H_2 molecules in the catalyst were the only parameter controlling the conversion efficiency, one would expect a linear decrease of the CE with increasing flow. Hence there must be additional mechanisms influencing the CE which could be, e.g., occupation of calibration sites or an inhomogeneous mixing within the catalyst.

Over longer time spans of several months, the CE can decrease significantly, strongly dependent on storage conditions, probably due to contamination of reaction sites on the Pt catalyst. Therefore, several treatments of the Pt mesh were tested in order to restore the reaction sites. We found that a simple roughening of the Pt surface, thereby physically removing contaminated spots on the surface, works best and can reliably restore optimal conversion conditions. However, the largest uncertainty in the calibration still arises from the stability of the $H_2 \rightarrow H_2O$ conversion on the catalyst. The calibration source is therefore regularly calibrated on ground during a campaign period, typically between every two flights. Including the uncertainty of the reference measurements (0.1 K in frost point, which translates to roughly

1 % relative accuracy in mixing ratio) and H_2O contamination in the H_2/ zero air mixture (stable at less than 0.5 ppmv, including bottle to bottle differences), the total accuracy of the in-flight calibration source is around 6 %.

A typical in-flight calibration sequence takes about 10–20 min, depending on the number of calibration steps. Due to the non-linearity of the calibration (see next section), at least three calibration steps are required in order to obtain a reliable calibration function. If there is enough time during a specific flight sequence, usually five to six calibration steps are performed in order to assure quality and consistency of the calibration. For all steps the flow of the calibration gas is higher than the sampling flow into the instrument. The excess flow is drained through the inlet.

4 Custom gas-discharge ion source

The ion source is an essential part of the mass spectrometer since its geometry and the ionization mechanism determine the type and amount of product ions used for the detection of trace gases. For AIMS we use different DC gas-discharge ion sources which were developed specifically for the different AIMS configurations. The gas-discharge ion source and the resulting ionization process is one of the major differences between AIMS and the CIMS-H_2O instrument developed by Thornberry et al. (2013). Here, we describe the ion source setup for the AIMS-H_2O configuration.

4.1 Mechanical and electrical setup

Both ion sources utilize an electrical discharge between a gold needle at high potential and a wall or aperture held near ground. The physical design of the ion source is inspired by the work of Kürten et al. (2011), who described a discharge ion source using a gold needle at atmospheric pressures. In contrast to Kürten et al. (2011), the geometry, flow conditions and pressure are adapted for AIMS. Since the pressure in the ion source is significantly lower (4–40 hPa), the ionization mechanism for AIMS differs from Kürten et al. (2011). The setup for the ion source of AIMS-H_2O is shown in Fig. 5. The ionization is realized by applying a positive high voltage (HV) potential to a gold needle (Moxom SP-X Gold, Moxom Acupuncture GmbH, Germany). The potential is provided by a HV module (DPp100504245M, iseg Spezialelektronik GmbH, Germany) and can be adjusted between 0 and 10 kV with a maximum current of 0.5 mA. The HV supply and needle are connected via a SHV (safe high voltage) vacuum feedthrough (SHV20, VACOM GmbH, Germany). Additionally, a 500 MΩ resistance is placed between the HV supply and needle in order to limit the current to 0.01 mA and prevent an uncontrolled self-maintaining discharge. The counter-electrode is the wall of the ion source. In order to control the initial electrical potential of the ions, the wall of the ion source can be set to a potential between −250 and +250 V.

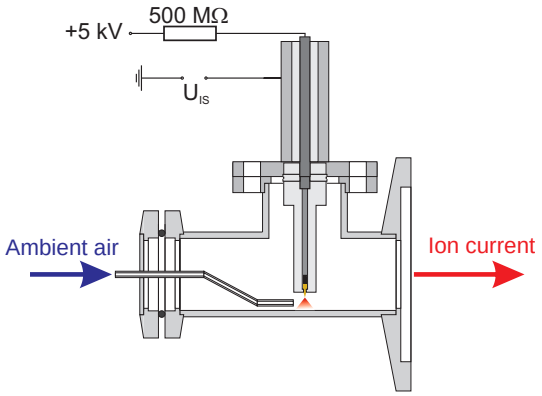

Figure 5. Gas-discharge ion source of AIMS-H_2O: ambient air is guided to the discharge zone between a gold needle and the wall of the source (red shaded region). The needle has a positive potential of +5 kV relative to the shielding of the assembly which itself can be set at variable potential vs. ground. A resistance of 500 MΩ is integrated in order to limit the maximum ion current to 0.01 mA.

The body of the ion source is a KF16 tee directly mounted to the mass spectrometer. Ambient air enters from the left-hand side and is guided to the discharge region (indicated in red). The fixture holding the gold needle (PEEK) is designed for a distance of 6 mm between needle and the wall of the ion source. In this setup, ambient air is ionized directly and guided to the first chamber of the MS. The HV supply is set to a positive potential of +5 kV; depending on the current, the potential between needle and wall is lower. The ion source pressure is controlled to 4.3 hPa corresponding to an atmospheric sample flow through the ion source of 0.9 standard L min^{-1}. The wall of the ion source is set to +4.0 V in order to accelerate the positive ions to the first pinhole held at +1.5 V. The ionization region itself can be divided into two parts. In the region in the direct vicinity of the needle tip, the electric field is strong enough to split neutral molecules into positive ions and electrons. There, negative ions and electrons are attracted by the needle tip and thus quickly removed from the gas phase. In the much larger region between needle and wall, the so-called ion drift region (Chen, 2002), positive ions are accelerated towards the wall. This is the region where water molecules react to form the detected product ions and ion–molecule clusters. The low pressure in the flow tube and the short distance to the mass spectrometer prevent further reactions of H_3O^+ ions with molecules of higher proton affinity as is typically used for ionization in Proton Transfer Reaction Mass Spectrometry. Thus the $H_3O^+(H_2O)_n$ product ions are not significantly consumed by subsequent chemical ionization.

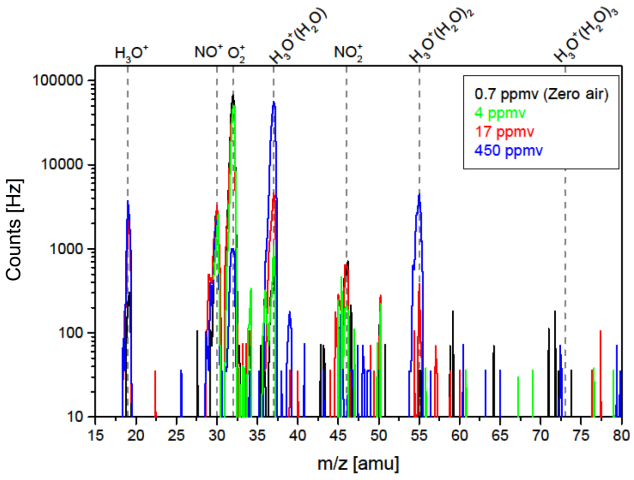

Figure 6. Mass spectra for m/z ratios from 15 to 80 amu for four different water vapor mixing ratios. The black curve represents a measurement of an added zero air flow, the other three spectra are samples of ambient atmospheric air during flight. As H_2O mixing ratios increase, the signals on H_3O^+, $H_3O^+(H_2O)$ and (@450 ppmv) $H_3O^+(H_2O)_2$ increase whereas the O_2^+ signal decreases. The signal on $H_3O^+(H_2O)_3$ does not increase up to mixing ratios of 450 ppmv. NO^+ and NO_2^+ stay almost constant over the range of water vapor mixing ratios shown here.

4.2 Ion reaction scheme for AIMS-H_2O

For the H_2O mode of AIMS, the ion–molecule reactions in the ion source are very similar to the reactions in the D region of the ionosphere (Thornberry et al., 2013). These reactions are described by, e.g., Fite (1969), Fehsenfeld et al. (1971) and Ferguson (1974). Due to the rapid transfer of charge from N_2^+ to O_2, the majority of positive ions entering the drift region are O_2^+ ions. After the three-body-collision reaction

$$O_2^+ + O_2 + M \rightarrow O_4^+ + M \qquad \text{(R1)}$$

including either neutral nitrogen or oxygen molecules ($k = 2.6 \times 10^{-30}\,(T/300)^{3.2}\,\mathrm{cm^6\,s^{-1}}$, Payzant et al., 1973), ambient water vapor reacts with O_4^+ to produce the primary product $H_3O^+(H_2O)$ via the following reactions:

$$O_4^+ + H_2O \rightarrow O_2^+(H_2O) + O_2 \qquad \text{(R2)}$$

$$O_2^+(H_2O) + H_2O \rightarrow H_3O^+(OH) + O_2 \qquad \text{(R3)}$$

$$H_3O^+(OH) + H_2O \rightarrow H_3O^+(H_2O) + OH. \qquad \text{(R4)}$$

Reactions (R2)–(R4) have similar high rate constants of the order of $k = 1.5 \times 10^{-9}\,\mathrm{cm^3\,s^{-1}}$ and are thus very fast (Ferguson, 1974). For that reason a short distance between the ionization region and the entrance pinhole of the mass spectrometer is sufficient for the H_2O configuration. For the quantitative measurement of atmospheric water vapor we use $H_3O^+(H_2O)$ as the primary product ion at a mass-to-charge ratio of 37 amu (atomic mass unit). Since the reaction from H_2O to $H_3O^+(H_2O)$ has multiple steps it cannot be considered as a first-order reaction. Thus the calibration of $H_3O^+(H_2O)$ vs. H_2O is expected to be non-linear. Moreover, we also observe higher clusters of H_3O^+ with increasing H_2O formed by the reaction suggested by Cunningham et al. (1972):

$$H_3O^+(H_2O)_{n-1} + H_2O + M \rightleftarrows H_3O^+(H_2O)_n + M. \qquad \text{(R5)}$$

In the upper troposphere and lower stratosphere, clusters with $n > 1$ do not contribute significantly to the observed H_3O^+ ion distribution. In more humid regions in the middle and lower troposphere, clusters with $n = 1$–3 show a significant signal. By using measurements of multiple clusters, AIMS-H_2O is able to measure water vapor from the lower troposphere up to the stratosphere.

Apart from the H_2O branch of reactions described above, there are also multiple reaction pathways to form NO^+ and NO_2^+ ions from the initial N_2^+ and O_2^+. Since nitrogen and oxygen are abundant in the atmosphere and no water vapor is included directly in these reactions, H_2O has only a small impact on NO_2^+ formation and an insignificant influence on NO^+. Thus, the signal of NO^+ at $m/z = 30$ amu is used as an independent measure of the stability of the ionization and ion–molecule reaction process. The signal of NO_2^+ is 1 order of magnitude lower than NO^+ and exhibits a slight anticorrelation with H_2O.

4.3 Mass spectrum for the detection of water vapor

The reactions described above can be directly linked to the mass spectra measured with AIMS-H_2O. Four typical spectra corresponding to different water vapor mixing ratios are shown in Fig. 5. In the mass range shown, all ions have a single positive charge, hence the mass-to-charge ratio is identical to the ion mass. The H_3O^+ ion at 19 amu exhibits a small positive correlation with H_2O, mainly due to fragmentation of $H_3O^+(H_2O)$ in the CDC. However, the overall signal is weak and not used for the evaluation of H_2O. NO^+ exhibits a stable moderate signal at 30 amu and, as noted above, is independent of ambient water vapor. As expected from Reactions (R1)–(R4) the signal of O_2^+ is very high at the lowest H_2O mixing ratios and anti-correlated with ambient water vapor since O_2^+ represents the source ion for the reaction with H_2O. Independent of the water vapor mixing ratio, we do not observe any significant signal on the intermediate ions from Reactions (R1)–(R4), namely O_4^+ ($m/z = 64$), $O_2^+(H_2O)$ ($m/z = 50$) and $H_3O^+(OH)$ ($m/z = 36$). This suggests that the intermediate states are rather short-lived and the reaction path (Reactions R1–R4) is already completed within the reaction chamber. As the reactions also suggest, the $H_3O^+(H_2O)$ ion at 37 amu shows the strongest correlation with water vapor, and its signal strength is comparable to that of the O_2^+ ion. At mixing ratios below 500 ppmv, the signal strength of higher clusters is more than one order of

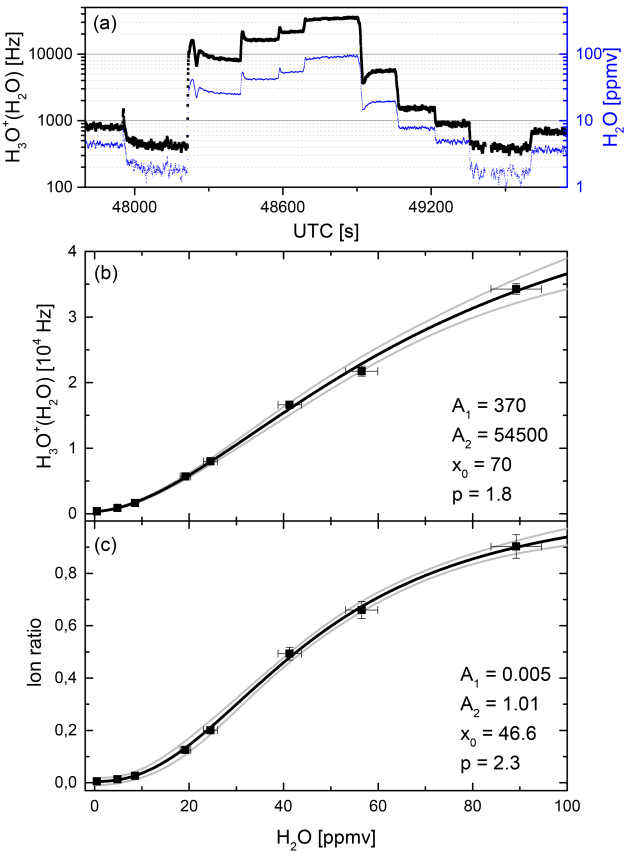

Figure 7. In-flight calibration curves for two different evaluation methods. **(a)** Time series of the $H_3O^+(H_2O)$ ($m/z = 37$ amu) signal for a characteristic calibration sequence. The corresponding water vapor mixing ratio, calculated from the AIMS-H_2O count rate, is shown in blue. **(b)** Count rate on $m/z = 37$ amu vs. H_2O in the calibration gas. In panel **(c)** the ratio of ion masses $(19+37+55)/(19+32+37+46+55)$ is plotted against H_2O. The gray curves mark the 95 % confidence interval of the respective fit curves, fit parameters are given for both calibration methods.

magnitude lower. Hence, the $H_3O^+(H_2O)$ signal can be used as direct measure for ambient water vapor mixing ratios. At H_2O mixing ratios above 500 ppmv, the higher clusters $H_3O^+(H_2O)_2$ at 55 amu and $H_3O^+(H_2O)_3$ at 73 amu become significant in terms of signal strength.

5 Two data evaluation methods

The data reduction procedure begins with the evaluation of a laboratory or in-flight calibration and an appropriate application of the calibration to the flight data. In a second step, corrections for dilution, cross-sensitivities or other influences on the measurement can be applied. For AIMS-H_2O we utilize two different methods to determine the atmospheric H_2O mixing ratio from the count rates measured by the mass spectrometer, both with benefits and disadvantages. Considering Reactions (R1)–(R4), a direct way to determine ambient H_2O is to calibrate the signal of the $H_3O^+(H_2O)$ on mass 37 amu at different water vapor mixing ratios. In doing so, one obtains a calibration as shown in Fig. 7b, derived from a typical calibration sequence (Fig. 7a). As expected from the multiple reaction steps to produce $H_3O^+(H_2O)$, the calibration function is non-linear. For water vapor mixing ratios below 30 ppmv, the number of H_2O molecules is the limiting factor. Since three water molecules are involved in the reaction pathway from O_2^+ to $H_3O^+(H_2O)$, the calibration curve has a cubic shape in that region. For high H_2O, the available number of O_2^+ ions becomes the limiting factor, until at a certain H_2O mixing ratio all O_2^+ ions are depleted by Reactions (R1)–(R4). Hence the cubic shape is expected to change into an exponential saturation. For H_2O mixing ratios > 500 ppmv in AIMS-H_2O, no new $H_3O^+(H_2O)$ ions are formed since O_2^+ is completely depleted. However, Reaction (R5) still alters the hydration of the existing ions towards higher clusters. In that region the amount of $H_3O^+(H_2O)_2$ and $H_3O^+(H_2O)_3$ increases at the expense of $H_3O^+(H_2O)$. Although the shape of the calibration curve can be well understood from the point of reaction kinetics, a fit with two different functions is rather impractical due to the high number of parameters and the uncertainty in the transition region. Therefore we apply a more pragmatic approach and use a logistic fit function:

$$y = \frac{A_1 - A_2}{1 + (x/x_0)^p} + A_2. \quad (1)$$

This function is an asymmetric S-shaped curve with an initial value A_1 at $x = 0$, a final value A_2 for $x \to \infty$, a center at x_0 and a power parameter p. This function combines the characteristic shapes observed in both regimes at mixing ratios < 30 ppmv and between 30 and 100 ppmv. Moreover, it has only four free parameters and can be inverted analytically, which makes it comfortable to handle. This evaluation method using only the $H_3O^+(H_2O)$ signal is referred to as method 1.

The confidence bands for method 1 (Fig. 7b) widen significantly when approaching mixing ratios of 50 ppmv and above, indicating an increasing uncertainty in the fit function and consequently in the determination of the ambient mixing ratio. Therefore, an alternative evaluation method is shown in Fig. 7c and referred to as method 2, which uses additional information provided by the signal of the other H_3O^+ clusters, NO_2^+ and most importantly O_2^+. The signal ion ratio is then calculated as

$$\mathrm{ir} = \frac{\sum_{n=0}^{2} [H_3O^+(H_2O)_n]}{[O_2^+] + [NO_2^+] + \sum_{n=0}^{2} [H_3O^+(H_2O)_n]}, \quad (2)$$

where the brackets symbolize the count rate on the respective ion mass. This method includes all ions with significant count rates that respond to changes in H_2O. The idea behind

Table 1. Measurement range, accuracy and precision for AIMS-H_2O. Remarks concern the parameters used to determine the precision and detection limit. For AIMS-H_2O, the two values for precision correspond to the two evaluation schemes using ion mass 37 amu ($H_3O^+(H_2O)$) and ion ratio, respectively.

	Sensitivity	Accuracy	Precision (%)		Remark
	(counts ppmv^{-1})	(%)	37 amu	ir	
Global (1–500 ppmv)	50–400	7–15	4–15	1.5–15	Precision for 4 Hz data
@ 5 ppmv (stratospheric)	180	7	10 (7)	15 (8)	Precision for both evaluation methods and 4 Hz (1 Hz) data
@ 100 ppmv (tropospheric)	400	11	6.5 (4.5)	2 (1.7)	Same as above with 1 : 1 dilution ratio

the approach is to normalize counts of all water-dependent ions to the overall ion counts offering some benefits compared to the single ion evaluation: (1) the signal to noise ratio is improved, (2) the method automatically accounts for any (e.g., temperature-induced) drifts in the efficiency of the ion source, (3) the confidence bands of the logistic fit for the in-flight calibration stay almost constant over the entire calibration range. However, as well as working for higher H_2O mixing ratios, the smaller slope of the calibration at mixing ratios below 15 ppmv increases the precision of the measurement in that region (Table 1). For mixing ratios between 15 and 70 ppmv, both evaluation methods agree within ± 5 %. In order to combine the benefits of both evaluation methods, we use the single ion method (method 1) for mixing ratios below 15 ppmv and the ion ratio method (method 2) for H_2O mixing ratios above 15 ppmv as explained in detail in the next section on instrumental uncertainties.

6 Data quality and sources of uncertainty

The data quality depends on various factors, with sensitivity of the instrument to a specific trace gas and signal noise being the most important ones. Additionally, any kind of drift effects modifying the count rates, cross-sensitivities and uncertainties in the in-flight calibration change the data quality. In this work, we performed an extensive analysis of possible sources of uncertainty which is necessary to judge the reliability of the H_2O measurements in the atmosphere.

6.1 Sensitivity and detection limits

For the determination of signal noise, the in-flight calibration sequences are the most useful data since they are free of atmospheric variability and usually exhibit periods with stable signal long enough for sufficient statistics. The signal noise is best described by the standard deviation of the count rate, which increases with the absolute signal. Starting from an idealized statistical approach, the ion count rates can be described by a Poisson distribution. Hence, the standard deviation of the signal should equal the square root of the count rate. In reality, instrumental factors like variability of the discharge in the ion source, the transmission of the quadrupole and electrical noise from the detector increase the signal noise compared to the idealized value. For the complete AIMS setup, all these factors increase the signal noise roughly by a factor of 2 compared to pure statistical noise from Poisson theory.

However, data quality is not only determined by signal noise but equally by the instrument's sensitivity. For a linear calibration, sensitivity and signal noise are usually used to determine the detection limit (MacDougall and Crummett, 1980). The detection limit is the value below which the signal cannot be distinguished statistically from the background noise within a certain statistical significance. Assuming a constant calibration factor CF and a standard deviation σ_0 of the zero air signal, the detection limit DL is defined as

$$\mathrm{DL} = \mathrm{CF} \times \sigma_0. \tag{3}$$

The classical combination of sensitivity and detection limit cannot be directly transferred to the water vapor measurements with AIMS-H_2O for two reasons. First, the calibration is non-linear, hence sensitivity depends on the actual water vapor mixing ratio. Second, the detection limit is not a useful parameter for water vapor since even the lowest mixing ratios prevalent in the atmosphere exceed the detection limit by at least 1 order of magnitude. Hence, for water vapor we apply a different approach evaluating sensitivity (defined as the first derivative of the calibration curve) and signal noise as a function of the water vapor mixing ratio $\langle H_2O \rangle$. We define the effective sensitivity by the ratio of the sensitivity and noise as a function of $\langle H_2O \rangle$:

$$\mathrm{ES}(\langle H_2O \rangle) = \frac{\frac{\partial [H_3O^+(H_2O)]}{\partial \langle H_2O \rangle}(\langle H_2O \rangle)}{\sigma_{H_3O^+(H_2O)}(\langle H_2O \rangle)}. \tag{4}$$

This definition is similar to the classical signal-to-noise ratio but accounts for the change in sensitivity depending on the ambient water vapor mixing ratio. For the evaluation method 1, the ES reaches its highest values of 1.3 ppmv^{-1} for low water vapor mixing ratios of around 5 ppmv (Fig. 8), which are typical values for the lower stratosphere. At lower

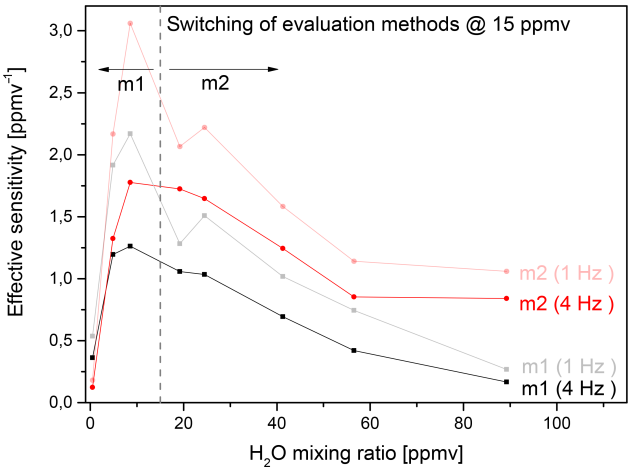

Figure 8. Effective sensitivity, as defined in Eq. (4), for evaluation method 1 (black) and method 2 (red). ES increases up to ∼ 10 ppmv due to the increase in the slope of the calibration curve. At higher mixing ratios, the decrease of ES is caused by increasing signal noise. Below 15 ppmv, method 1 is used for calculation of atmospheric mixing ratios; above 15 ppmv, method 2 is used.

H_2O mixing ratios, the ES decreases due to the decrease in the slope of the calibration curve. At higher mixing ratios, the ES is lowered by increasing signal noise and additionally by decreasing sensitivity at the upper end of the calibration range. Using 1 Hz data for the calculation of the ES instead of the 4 Hz data, the ES is higher by a factor of 1.3–1.5.

The ES can equally be calculated for method 2 by replacing the count rate [$H_3O^+(H_2O)$] by the ion ratio ir (red lines in Fig. 8). Comparing the ES values for both evaluation methods one obtains a measure of which method provides better data quality in a certain mixing ratio range. As can be expected from the shape of the calibration curve in Fig. 7c, the smaller slope at very low mixing ratios results in a reduced ES for the ratio approach in that region. At higher mixing ratios, the ES using method 2 is a factor of 1.5 (at 35 ppmv) to 4 (at 120 ppmv) higher than that using the single ion evaluation. Hence this method provides better data quality in this region. Although the ES is higher for method 2 compared to method 1 already at mixing ratios above 2 ppmv, in practice method 1 (Fig. 8), using the $H_3O^+(H_2O)$ count rate only, is more reliable and stable for mixing ratios below 15 ppmv. A possible reason for this might be that at low mixing ratios there is a large abundance of O_2^+ product ions. Thus, the reaction of H_2O to $H_3O^+(H_2O)$ is almost independent of the actual number of O_2^+ ions. When including the O_2^+ count rate in the data evaluation process, fluctuations in the O_2^+ count rate (e.g., temperature induced) are likely to be incorrectly interpreted as a water vapor signal. That increases the uncertainty of the measurement rather than providing an additional source of information as it does for the higher mixing ratios.

6.2 Instrumental uncertainties

In addition to the uncertainty arising from the calibration procedure, the fitting procedures and the approximations in data evaluation, a couple of other effects can lead to an increased uncertainty of the measurement with AIMS.

One factor increasing measurement uncertainty is an observed dependence of the quadrupole transmission on the cabin temperature in the aircraft. The control electronics for the oscillating circuit are found to decrease the ion transmission through the quadrupole with increasing cabin temperature. Since this effect applies to all measured ions, the evaluation methods using absolute ion counts for AIMS-H_2O is affected most. Methods using ion ratios are only affected by a mass- or count rate-dependence in the change in ion counts. During flight, the effect is of minor importance since the air conditioning provides a fairly stable (±1 °C) temperature environment. However, the temperature dependence is identified to be a major cause for the observed discrepancy between airborne and ground measurements. The temperature dependence is hard to quantify in laboratory measurements, but is addressed by a thorough in-flight calibration of the instrument.

A second important point influencing the measurement is the possible artifact created by water desorbing slowly from the walls of the vacuum chamber. In contrast to laboratory measurements where the turbomolecular pumps run continuously for several days, the chamber must be pumped down before every flight. This takes around 3 h prior to takeoff in order to achieve stable vacuum conditions. Between the flights, the vacuum chamber is either sealed under vacuum or filled with dry nitrogen. Both procedures result in a similar time needed for the subsequent evacuation of the chamber.

Not only the vacuum chamber, but also the inlet line can be contaminated with water vapor and other trace gases. In order to minimize the effect of moisture in the inlet, the whole inlet line is routinely flushed with dry nitrogen during taxi and takeoff. Since components of the flow system with high surface areas, such as the pressure regulation valve, exhibit a passivation and hysteresis which can change typical response times by up to a factor of 3, the effect depends on the measurement history.

Overall, the accuracy of the instrument is determined to be between 7 and 15 %, where the uncertainty of the in-flight calibration and the dilution correction are the major contributors. The best accuracy can be achieved in the range between 10 and 40 ppmv H_2O where the instrument is most sensitive. For lower mixing ratios, the relative accuracy increases due to error sources with constant contribution – e.g., offsets in the mixing ratio of the calibration flow. At higher mixing ratios, the accuracy decreases mainly due to an increased uncertainty in the conversion efficiency of the catalytic water vapor source and due to the dilution correction.

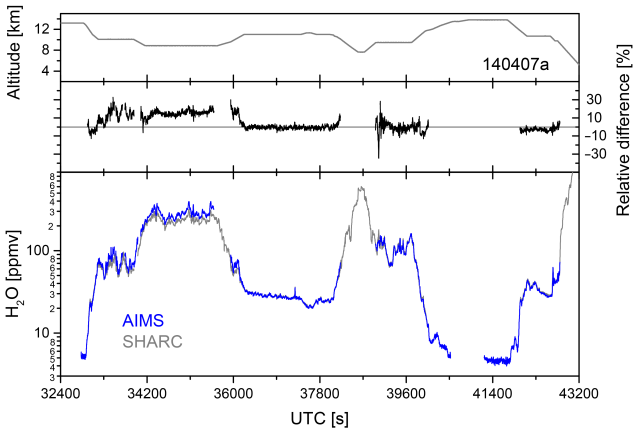

Figure 9. Time series of H_2O mixing ratio (bottom panel) from a flight on 7 April 2014 during the ML-CIRRUS campaign. The blue curve is the gas phase measurement of AIMS-H_2O. For comparison, measured mixing ratios from the SHARC TDL (gray) are shown. For the high mixing ratios between 34 000 and 35 600 s, the sample flow of AIMS-H_2O was diluted with synthetic air. The top panel shows the flight altitude, the middle panel denotes the relative difference between both instruments. Data from both instruments agree reasonably well.

6.3 Cross-sensitivity

We investigated the cross-sensitivity of selected trace gases on H_2O detected with AIMS-H_2O. We observed no significant cross-sensitivity of ozone, which is consistent with previous investigations (Thornberry et al., 2013). In the same study, they found a very small influence of CH_4 of about 1 % of the sensitivity on H_2O on their H_3O^+ signal. Given typical ambient CH_4 concentrations of around 1.8 ppmv, we obtain a possible bias of 0.018 ppmv which is much smaller than the dominant sources of uncertainty of the in-flight measurements. For CO_2, Thornberry et al. (2013) reported a decrease in sensitivity of around 10 % when adding ambient CO_2 mixing ratios of 380 ppmv to the sample flow. In order to evaluate the possible influence of CO_2 for the different ionization source we use here, two separate calibrations with and without CO_2 were performed with AIMS-H_2O. In these calibrations, we did not observe any change in sensitivity of the $H_3O^+(H_2O)$ ion with or without additional CO_2.

7 Flight performance of AIMS-H_2O on HALO during ML-CIRRUS

AIMS-H_2O flew on the DLR Falcon in 2011 (Kaufmann et al., 2014; Voigt et al., 2014) and on HALO during the ML-CIRRUS experiment in March/April 2014. In order to provide an example of the performance of AIMS-H_2O, the water vapor time series of flight 9 on 7 April 2014 is shown in Fig. 9. The scope of this flight was to study contrail cirrus above Germany. The contrail cirrus were embedded in a frontal cirrus system extending above western and eastern Germany. In addition, we planned an intercomparison with ground-based lidar measurements in Munich and Leipzig and with data from a radiosonde launched in Lindenberg. To this end, HALO took off from Oberpfaffenhofen, near Munich, at 07:00 UT and performed three transects in the heavily traveled airspace between Frankfurt and Berlin before returning to Oberpfaffenhofen. Two transects were selected for in situ measurements of contrail cirrus and natural cirrus while the third stratospheric transect focused on remote sensing of the cirrus/contrail cirrus clouds with the onboard lidar system. Hence, in this flight we performed measurements inside cirrus clouds and in cloud-free air at a range of water vapor mixing ratios down to 4 ppmv.

Besides data from AIMS-H_2O, H_2O mixing ratios measured by the tunable diode laser hygrometer SHARC are shown in Fig. 9. SHARC is regularly calibrated on the ground using a MBW373-LX as reference, and has been shown to agree well with the established hygrometer FISH (Meyer et al., 2015). Both instruments measured gas phase water vapor via an actively pumped backward-facing inlet. The agreement between the two instruments is excellent at water vapor mixing ratios below 150 ppmv during a large part of the flight after 36 000 s UTC. In particular, at H_2O mixing ratios down to 10 ppmv, the agreement is within ±5 %. Since the measurement range of the SHARC instrument is limited to mixing ratios above 10 ppmv, no comparison could be done for the flight legs in the lower stratosphere.

At the beginning of the flight between 33 300 s and 35 600 s UT, H_2O mixing ratios measured by AIMS-H_2O were 12–15 % higher than the SHARC data, while short-timescale H_2O variations were very similar. We speculate that AIMS-H_2O might overestimate the water vapor mixing ratio near 300 ppmv during that flight sequence due to a bias in the dilution correction. This effect is not permanent, but rather a feature observed only during that flight. However, the deviations are still within the combined uncertainty of both instruments (10 % for SHARC). Regarding the relative humidity with respect to ice (RHi) derived from H_2O mixing ratios and static air temperature measurements from HALO, AIMS measured a slight mean supersaturation with respect to ice in that sequence while SHARC measured a slight mean subsaturation (lower panel in Fig. 10). Both instruments detected rapid fluctuations in RHi between 60 and 140 %. Here we use the ice water content (IWC) calculated from the total water measurement by the Water vapouR Analyzer (WARAN) tunable diode laser instrument (Groß et al., 2014) as an indicator for the occurrence of cirrus clouds (top panel in Fig. 10). The large variation in IWC suggests that we sampled a rather inhomogeneous cirrus cloud during the sequence from 33 300 to 35 600 s, which is consistent with the scatter of RHi around saturation. In later parts of the measurement sequence in Fig. 10 (36 000–38 000 s), the IWC suggests a more dense and homogeneous cloud while both AIMS and SHARC indicate a mean subsaturation at

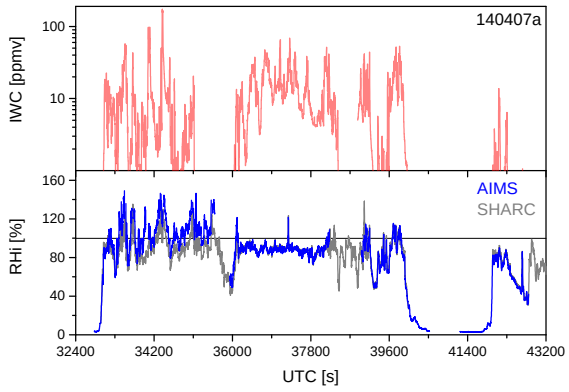

Figure 10. Top: ice water content (IWC) as cloud marker derived from total water measurements by the WARAN tunable diode laser instrument. Bottom: relative humidity with respect to ice calculated from AIMS H_2O mixing ratios (blue curve) and SHARC mixing ratios (gray curve) using the HALO static air temperature measurement. Except for the middle part from 36 000 to 38 000 s where the in-cloud RHi is below 100 %, RHi typically scatters around saturation inside the clouds.

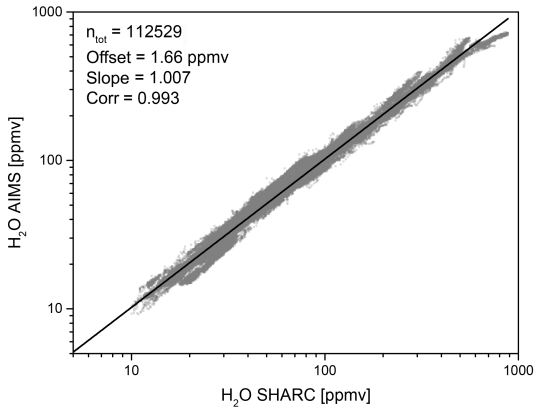

Figure 11. H_2O mixing ratio of AIMS-H_2O plotted versus the mixing ratio measured by SHARC with data from the entire ML-CIRRUS campaign (gray dots). Offset, slope and correlation coefficient of the linear fit function (black line) indicate an excellent overall agreement between both instruments.

around 91 % RHi. For the two following cirrus penetrations at 37 000 and 37 800 s, RHi again fluctuates around saturation in both water vapor instruments. The uncertainty of RHi ($\sim$ 15–20 %) is almost equally distributed between uncertainty of the H_2O gas phase measurement and the uncertainty of the static temperature measurement made from the aircraft (0.5 K).

In order to obtain a quantitative impression of the instrument performance over the entire campaign, Fig. 11 shows a scatter plot of H_2O mixing ratios measured by AIMS-H_2O and SHARC with an extensive set of 112 529 data points gathered in March/April 2014. The linear fit ($H_2O(\mathrm{AIMS}) = 1.007 \times H_2O(\mathrm{SHARC}) + 1.66$ ppmv) shows the excellent overall agreement between the instruments, with a very high correlation coefficient of 0.993 giving high confidence in the data quality from both AIMS-H_2O and SHARC. The scatter of the data is comparable to the intercomparison published by Rollins et al. (2014).

While this paper focuses on the instrument description of AIMS-H_2O, a further detailed intercomparison of the set of water vapor instruments participating in ML-CIRRUS is beyond the scope of this paper and will be published elsewhere.

8 Summary and outlook

With the airborne mass spectrometer AIMS, we developed a measurement technique to quantify low water vapor mixing ratios typical for the upper troposphere and lower stratosphere. To this end, we built a new gas discharge ion source which directly ionizes ambient air sampled via a backward facing inlet. In a multi-step reaction similar to the reactions in the D-region of the ionosphere, water vapor molecules in ambient air react to $H_3O^+(H_2O)_n$ ($n = 0 \ldots 3$) ions which are detected by the mass spectrometer. We perform a comprehensive and in-depth error analysis and achieve a high accuracy between 7 and 15 % in the measurement range between 1 and 500 ppmv, depending on specific humidity and time resolution of the measurement. The accuracy is established by regular in-flight calibration of the instrument using a water vapor standard generated by the catalytic reaction of hydrogen and oxygen on a heated Pt surface.

In order to increase the signal quality, two different data evaluation methods are used to determine ambient water vapor mixing ratios from the respective ion count rates. For water vapor mixing ratios below 15 ppmv, we use the count rate of $H_3O^+(H_2O)$ at $m/z = 37$ to determine atmospheric water vapor. For higher mixing ratios, a normalized signal including all water vapor dependent ions provides better data quality. Major other contributors to uncertainty in the measurement are contamination of the vacuum chamber and inlet line with water vapor, and especially the temperature dependence of the quadrupole transmission.

AIMS-H_2O has been successfully deployed on the two DLR research aircraft Falcon and HALO during CONCERT in 2011 and ML-CIRRUS in 2014, where the comparison with airborne TDL hygrometer SHARC showed reasonable agreement within ± 10 % for most of the data.

During the CONCERT 2011 mission, AIMS-H_2O data proved to be well suited for accurate measurements of relative humidity in contrails and contrail cirrus environments (Kaufmann et al., 2014). In future, open questions regarding contrail microphysics (Voigt et al., 2011; Jeßberger et al., 2013; Schumann et al., 2013) and the persistence of contrails (Gayet et al., 2012; Kübbeler et al., 2011) will be addressed

using ML-CIRRUS data from AIMS-H_2O. In addition, we will perform a thorough intercomparison of the set of water vapor instruments operated on HALO to assess the quality of water vapor in situ measurements in the lower stratosphere in mid-latitudes. These data will help to better quantify uncertainties in H_2O mixing ratios in mid-latitudes, similar to the assessment of Rollins et al. (2014). With the 4 Hz time resolution, water vapor and supersaturation fluctuations can be investigated at spatial scales of the order of 50 m (Kärcher et al., 2014).

Including H_2O measurements with a frost point hygrometer (Voigt et al., 2010) from a series of campaigns, we envisage constructing a database of high-quality in situ H_2O measurements in the UTLS which can be used for comparison with lidar observations (Groß et al., 2014), meteorological and balloon sondes (Hurst et al., 2011), satellite data (Hegglin et al., 2013) and for model validation (Hegglin et al., 2014; Solomon et al., 2010). With the flexible airborne mass spectrometer AIMS, we have developed a multitool to address key issues concerning atmospheric composition of the UTLS and processes related to trace gas transport, cloud formation and climate.

Acknowledgements. We thank the German Science Foundation DFG for funding within HALO-SPP 1294 under contract VO 1504/2-1. Christiane Voigt, Stefan Kaufmann and Tina Jurkat are grateful for financing by the Helmholtz Association under contract VH-NG-309 and under contract W2/W3-60. We thank Andreas Minikin, Ulrich Schumann and DLR Flight Experiments for the coordination and realization of the ML-CIRRUS campaign and Greta Stratmann for helpful comments on the paper.

The article processing charges for this open-access publication were covered by a Research Centre of the Helmholtz Association.

Edited by: D. Baumgardner

References

Chen, J.: Direct Current Corona-Enhanced Chemical Reactions, PhD Thesis, Department of Mechanical Engineering, University of Minnesota, 2002.

Cunningham, A. J., Payzant, J. D., and Kebarle, P.: Kinetic study of the proton hydrate $H^+(H_2O)_n$ equilibriums in the gas phase, J. Am. Chem. Soc., 94, 7627–7632, doi:10.1021/ja00777a003, 1972.

Dinh, T. and Fueglistaler, S.: Microphysical, radiative, and dynamical impacts of thin cirrus clouds on humidity in the tropical tropopause layer and lower stratosphere, Geophys. Res. Lett., 41, 6949–6955, doi:10.1002/2014GL061289, 2014.

Dinh, T., Fueglistaler, S., Durran, D., and Ackerman, T.: Cirrus and water vapour transport in the tropical tropopause layer – Part 2: Roles of ice nucleation and sedimentation, cloud dynamics, and moisture conditions, Atmos. Chem. Phys., 14, 12225–12236, doi:10.5194/acp-14-12225-2014, 2014.

Fahey, D. W., Gao, R.-S., Möhler, O., Saathoff, H., Schiller, C., Ebert, V., Krämer, M., Peter, T., Amarouche, N., Avallone, L. M., Bauer, R., Bozóki, Z., Christensen, L. E., Davis, S. M., Durry, G., Dyroff, C., Herman, R. L., Hunsmann, S., Khaykin, S. M., Mackrodt, P., Meyer, J., Smith, J. B., Spelten, N., Troy, R. F., Vömel, H., Wagner, S., and Wienhold, F. G.: The AquaVIT-1 intercomparison of atmospheric water vapor measurement techniques, Atmos. Meas. Tech., 7, 3177–3213, doi:10.5194/amt-7-3177-2014, 2014.

Fehsenfeld, F. C., Mosesman, M., and Ferguson, E. E.: Ion-molecule reactions in an O_2^+-H_2O system, J. Chem. Phys., 55, 2115–2120, doi:10.1063/1.1676382, 1971.

Ferguson, E. E.: Laboratory measurements of ionospheric ion-molecule reaction rates, Rev. Geophys. Space Phys., 12, 703–713, doi:10.1029/RG012i004p00703, 1974.

Fite, W. L.: Positive ion reactions, Can. J. Chem., 47, 1797–1807, doi:10.1139/v69-292, 1969.

Forster, P. M. D. and Shine, K. P.: Assessing the climate impact of trends in stratospheric water vapor, Geophys. Res. Lett., 29, 1086, doi:10.1029/2001gl013909, 2002.

Gayet, J.-F., Shcherbakov, V., Voigt, C., Schumann, U., Schäuble, D., Jessberger, P., Petzold, A., Minikin, A., Schlager, H., Dubovik, O., and Lapyonok, T.: The evolution of microphysical and optical properties of an A380 contrail in the vortex phase, Atmos. Chem. Phys., 12, 6629–6643, doi:10.5194/acp-12-6629-2012, 2012.

Groß, S., Wirth, M., Schäfler, A., Fix, A., Kaufmann, S., and Voigt, C.: Potential of airborne lidar measurements for cirrus cloud studies, Atmos. Meas. Tech., 7, 2745–2755, doi:10.5194/amt-7-2745-2014, 2014.

Hansel, A., Jordan, A., Holzinger, R., Prazeller, P., Vogel, W., and Lindinger, W.: Proton transfer reaction mass spectrometry: online trace gas analysis at the ppb level, Int. J. Mass Spectrom., 149–150, 609–619, doi:10.1016/0168-1176(95)04294-U, 1995.

Hegglin, M. I., Tegtmeier, S., Anderson, J., Froidevaux, L., Fuller, R., Funke, B., Jones, A., Lingenfelser, G., Lumpe, J., Pendlebury, D., Remsberg, E., Rozanov, A., Toohey, M., Urban, J., von Clarmann, T., Walker, K. A., Wang, R., and Weigel, K.: SPARC Data Initiative: comparison of water vapor climatologies from international satellite limb sounders, J. Geophys. Res., 118, 11824–11846, doi:10.1002/jgrd.50752, 2013.

Hegglin, M. I., Plummer, D. A., Shepherd, T. G., Scinocca, J. F., Anderson, J., Froidevaux, L., Funke, B., Hurst, D., Rozanov, A., Urban, J., von Clarmann, T., Walker, K. A., Wang, H. J., Tegtmeier, S., and Weigel, K.: Vertical structure of stratospheric water vapour trends derived from merged satellite data, Nat. Geosci., 7, 768–776, doi:10.1038/ngeo2236, 2014.

Heymsfield, A. J. and Miloshevich, L. M.: Relative humidity and temperature influences on cirrus formation and evolution: observations from wave clouds and FIRE II, J. Atmos. Sci., 52, 4302–4326, doi:10.1175/1520-0469(1995)052<4302:rhatio>2.0.co;2, 1995.

Huey, L. G. and Lovejoy, E. R.: Reactions of SiF_5^- with atmospheric trace gases: ion chemistry for chemical ionization detection of HNO_3 in the troposphere, Int. J. Mass. Spectrom., 155, 133–140, 1996.

Huey, L. G., Hanson, D. R., and Howard, C. J.: Reactions of SF_6^- and I^- with atmospheric trace gases, J. Phys. Chem., 99, 5001–5008, doi:10.1021/j100014a021, 1995.

Hurst, D. F., Oltmans, S. J., Vomel, H., Rosenlof, K. H., Davis, S. M., Ray, E. A., Hall, E. G., and Jordan, A. F.: Stratospheric water vapor trends over Boulder, Colorado: analysis of the 30 year Boulder record, J. Geophys. Res., 116, D02306, doi:10.1029/2010jd015065, 2011.

Jensen, E. J., Kinne, S., and Toon, O. B.: Tropical cirrus cloud radiative forcing – sensitivity studies, Geophys. Res. Lett., 21, 2023–2026, doi:10.1029/94gl01358, 1994.

Jensen, E. J., Smith, J. B., Pfister, L., Pittman, J. V., Weinstock, E. M., Sayres, D. S., Herman, R. L., Troy, R. F., Rosenlof, K., Thompson, T. L., Fridlind, A. M., Hudson, P. K., Cziczo, D. J., Heymsfield, A. J., Schmitt, C., and Wilson, J. C.: Ice supersaturations exceeding 100 % at the cold tropical tropopause: implications for cirrus formation and dehydration, Atmos. Chem. Phys., 5, 851–862, doi:10.5194/acp-5-851-2005, 2005.

Jeßberger, P., Voigt, C., Schumann, U., Sölch, I., Schlager, H., Kaufmann, S., Petzold, A., Schäuble, D., and Gayet, J.-F.: Aircraft type influence on contrail properties, Atmos. Chem. Phys., 13, 11965–11984, doi:10.5194/acp-13-11965-2013, 2013.

Jurkat, T., Voigt, C., Kaufmann, S., Zahn, A., Sprenger, M., Hoor, P., Bozem, H., Müller, S., Dörnbrack, A., Schlager, H., Bönisch, H., and Engel, A.: A quantitative analysis of stratospheric HCl, HNO_3, and O_3 in the tropopause region near the subtropical jet, Geophys. Res. Lett., 41, 3315–3321, doi:10.1002/2013GL059159, 2014.

Jurkat, T., Kaufmann, S., Voigt, C., Schäuble, D., Jeßberger, P., and Ziereis, H.: The airborne mass spectrometer AIMS – Part 2: Measurements of trace gases with stratospheric or tropospheric origin in the UTLS, Atmos. Meas. Tech., in press, 2016.

Kärcher, B., Dörnbrack, A., and Sölch, I.: Supersaturation variability and cirrus ice crystal size distributions, J. Atmos. Sci., 71, 2905–2926, doi:10.1175/JAS-D-13-0404.1, 2014.

Kaufmann, S., Voigt, C., Jeßberger, P., Jurkat, T., Schlager, H., Schwarzenboeck, A., Klingebiel, M., and Thornberry, T.: In situ measurements of ice saturation in young contrails, Geophys. Res. Lett., 41, 702–709, doi:10.1002/2013GL058276, 2014.

Kiehl, J. T. and Trenberth, K. E.: Earth's annual global mean energy budget, B. Am. Meteorol. Soc., 78, 197–208, doi:10.1175/1520-0477(1997)078<0197:eagmeb>2.0.co;2, 1997.

Krämer, M., Schiller, C., Afchine, A., Bauer, R., Gensch, I., Mangold, A., Schlicht, S., Spelten, N., Sitnikov, N., Borrmann, S., de Reus, M., and Spichtinger, P.: Ice supersaturations and cirrus cloud crystal numbers, Atmos. Chem. Phys., 9, 3505–3522, doi:10.5194/acp-9-3505-2009, 2009.

Kübbeler, M., Hildebrandt, M., Meyer, J., Schiller, C., Hamburger, Th., Jurkat, T., Minikin, A., Petzold, A., Rautenhaus, M., Schlager, H., Schumann, U., Voigt, C., Spichtinger, P., Gayet, J.-F., Gourbeyre, C., and Krämer, M.: Thin and subvisible cirrus and contrails in a subsaturated environment, Atmos. Chem. Phys., 11, 5853–5865, doi:10.5194/acp-11-5853-2011, 2011.

Kürten, A., Rondo, L., Ehrhart, S., and Curtius, J.: Performance of a corona ion source for measurement of sulfuric acid by chemical ionization mass spectrometry, Atmos. Meas. Tech., 4, 437–443, doi:10.5194/amt-4-437-2011, 2011.

Liou, K. N.: Influence of cirrus clouds on weather and climate processes – a global perspective, Mon. Weather Rev., 114, 1167–1199, doi:10.1175/1520-0493(1986)114<1167:ioccow>2.0.co;2, 1986.

MacDougall, D. and Crummett, W. B.: Guidelines for data acquisition and data quality evaluation in environmental chemistry, Anal. Chem., 52, 2242–2249, doi:10.1021/ac50064a004, 1980.

Manabe, S. and Wetherald, R. T.: Thermal equilibrium of the atmosphere with a given distribution of relative humidity, J. Atmos. Sci., 24, 241–259, doi:10.1175/1520-0469(1967)024<0241:teotaw>2.0.co;2, 1967.

McCrumb, J. L. and Arnold, F.: High-sensitivity detection of negative ions in the stratosphere, Nature, 294, 136–139, 1981.

Meyer, J., Rolf, C., Schiller, C., Rohs, S., Spelten, N., Afchine, A., Zöger, M., Sitnikov, N., Thornberry, T. D., Rollins, A. W., Bozóki, Z., Tátrai, D., Ebert, V., Kühnreich, B., Mackrodt, P., Möhler, O., Saathoff, H., Rosenlof, K. H., and Krämer, M.: Two decades of water vapor measurements with the FISH fluorescence hygrometer: a review, Atmos. Chem. Phys., 15, 8521–8538, doi:10.5194/acp-15-8521-2015, 2015.

Oltmans, S., Rosenlof, K., Michelsen, H., Nedoluha, G., Pan, L., Read, W., Remsberg, E., and Schiller, C.: SPARC Report No. 2: Upper Tropospheric and Stratospheric Water Vapour: Chapter 2, 2000.

Payzant, J. D., Cunningham, A. J., and Kebarle, P.: Temperature dependence of the rate constants for the third order reactions: $O_2^+ + 2O_2 = O_4^+ + O_2$ and $O_4^+ + 2O_2 = O_6^+ + O_2$, J. Chem. Phys., 59, 5615–5619, doi:10.1063/1.1679914, 1973.

Ramanathan, V., Cess, R. D., Harrison, E. F., Minnis, P., Barkstrom, B. R., Ahmad, E., and Hartmann, D.: Cloud-radiative forcing and climate – results from the Earth Radiation Budget Experiment, Science, 243, 57–63, doi:10.1126/science.243.4887.57, 1989.

Riese, M., Ploeger, F., Rap, A., Vogel, B., Konopka, P., Dameris, M., and Forster, P.: Impact of uncertainties in atmospheric mixing on simulated UTLS composition and related radiative effects, J. Geophys. Res., 117, D16305, doi:10.1029/2012JD017751, 2012.

Rollins, A. W., Thornberry, T. D., Gao, R.-S., Hall, B. D., and Fahey, D. W.: Catalytic oxidation of H_2 on platinum: a robust method for generating low mixing ratio H_2O standards, Atmos. Meas. Tech., 4, 2059–2064, doi:10.5194/amt-4-2059-2011, 2011.

Rollins, A. W., Thornberry, T. D., Gao, R. S., Smith, J. B., Sayres, D. S., Sargent, M. R., Schiller, C., Krämer, M., Spelten, N., Hurst, D. F., Jordan, A. F., Hall, E. G., Vömel, H., Diskin, G. S., Podolske, J. R., Christensen, L. E., Rosenlof, K. H., Jensen, E. J., and Fahey, D. W.: Evaluation of UT/LS hygrometer accuracy by intercomparison during the NASA MACPEX mission, J. Geophys. Res., 119, 2013JD020817, doi:10.1002/2013JD020817, 2014.

Sassen, K. and Comstock, J. M.: A midlatitude cirrus cloud climatology from the facility for atmospheric remote sensing – Part III: Radiative properties, J. Atmos. Sci., 58, 2113–2127, doi:10.1175/1520-0469(2001)058<2113:amcccf>2.0.co;2, 2001.

Schumann, U., Jeßberger, P., and Voigt, C.: Contrail ice particles in aircraft wakes and their climatic importance, Geophys. Res. Lett., 40, 2867–2872, doi:10.1002/grl.50539, 2013.

Solomon, S., Rosenlof, K. H., Portmann, R. W., Daniel, J. S., Davis, S. M., Sanford, T. J., and Plattner, G. K.: Contributions of stratospheric water vapor to decadal changes in the rate of global warming, Science, 327, 1219–1223, doi:10.1126/science.1182488, 2010.

Thornberry, T. D., Rollins, A. W., Gao, R. S., Watts, L. A., Ciciora, S. J., McLaughlin, R. J., Voigt, C., Hall, B., and Fahey, D. W.: Measurement of low-ppm mixing ratios of water vapor in the upper troposphere and lower stratosphere using chemical ionization mass spectrometry, Atmos. Meas. Tech., 6, 1461–1475, doi:10.5194/amt-6-1461-2013, 2013.

Viggiano, A. A.: In situ mass spectrometry and ion chemistry in the stratosphere and troposphere, Mass Spectrom. Rev., 12, 115–137, doi:10.1002/mas.1280120203, 1993.

Voigt, C., Schumann, U., Jurkat, T., Schäuble, D., Schlager, H., Petzold, A., Gayet, J.-F., Krämer, M., Schneider, J., Borrmann, S., Schmale, J., Jessberger, P., Hamburger, T., Lichtenstern, M., Scheibe, M., Gourbeyre, C., Meyer, J., Kübbeler, M., Frey, W., Kalesse, H., Butler, T., Lawrence, M. G., Holzäpfel, F., Arnold, F., Wendisch, M., Döpelheuer, A., Gottschaldt, K., Baumann, R., Zöger, M., Sölch, I., Rautenhaus, M., and Dörnbrack, A.: In-situ observations of young contrails – overview and selected results from the CONCERT campaign, Atmos. Chem. Phys., 10, 9039–9056, doi:10.5194/acp-10-9039-2010, 2010.

Voigt, C., Schumann, U., Jessberger, P., Jurkat, T., Petzold, A., Gayet, J. F., Kramer, M., Thornberry, T., and Fahey, D. W.: Extinction and optical depth of contrails, Geophys. Res. Lett., 38, L11806, doi:10.1029/2011gl047189, 2011.

Voigt, C., Jessberger, P., Jurkat, T., Kaufmann, S., Baumann, R., Schlager, H., Bobrowski, N., Giuffrida, G., and Salerno, G.: Evolution of CO_2, SO_2, HCl, and HNO_3 in the volcanic plumes from Etna, Geophys. Res. Lett., 41, 2196–2203, doi:10.1002/2013GL058974, 2014.

Vömel, H., David, D. E., and Smith, K.: Accuracy of tropospheric and stratospheric water vapor measurements by the cryogenic frost point hygrometer: instrumental details and observations, J. Geophys. Res., 112, D08305, doi:10.1029/2006jd007224, 2007.

Weinstock, E. M., Smith, J. B., Sayres, D. S., Pittman, J. V., Spackman, J. R., Hintsa, E. J., Hanisco, T. F., Moyer, E. J., St Clair, J. M., Sargent, M. R., and Anderson, J. G.: Validation of the Harvard Lyman-alpha in situ water vapor instrument: implications for the mechanisms that control stratospheric water vapor, J. Geophys. Res., 114, D23301, doi:10.1029/2009jd012427, 2009.